

The Substrate Capture Mechanism of *Mycobacterium tuberculosis* Anthranilate Phosphoribosyltransferase Provides a Mode for Inhibition

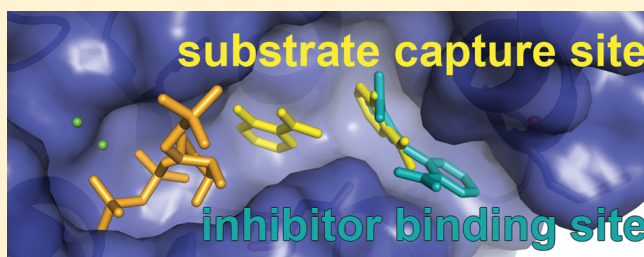
Alina Castell,^{†,§} Francesca L. Short,^{†,||} Genevieve L. Evans,[†] Tammie V. M. Cookson,[‡] Esther M. M. Bulloch,[†] Dmitri D. A. Joseph,[‡] Clare E. Lee,[†] Emily J. Parker,[‡] Edward N. Baker,[†] and J. Shaun Lott^{*,†}

[†]Maurice Wilkins Centre for Molecular Biodiscovery and School of Biological Sciences, University of Auckland, 3 Symonds Street, Auckland 1142, New Zealand

[‡]Maurice Wilkins Centre for Molecular Biodiscovery and Department of Chemistry, University of Canterbury, 20 Kirkwood Avenue, Christchurch 8140, New Zealand

S Supporting Information

ABSTRACT: Anthranilate phosphoribosyltransferase (AnPRT, EC 2.4.2.18) is a homodimeric enzyme that catalyzes the reaction between 5'-phosphoribosyl 1'-pyrophosphate (PRPP) and anthranilate, as part of the tryptophan biosynthesis pathway. Here we present the results of the first chemical screen for inhibitors against *Mycobacterium tuberculosis* AnPRT (*Mtb*-AnPRT), along with crystal structures of *Mtb*-AnPRT in complex with PRPP and several inhibitors. Previous work revealed that PRPP is bound at the base of a deep cleft in *Mtb*-AnPRT and predicted two anthranilate binding sites along the tunnel leading to the PRPP binding site. Unexpectedly, the inhibitors presented here almost exclusively bound at the entrance of the tunnel, in the presumed noncatalytic anthranilate binding site, previously hypothesized to have a role in substrate capture. The potencies of the inhibitors were measured, yielding K_i values of 1.5–119 μM , with the strongest inhibition displayed by a bianthranilate compound that makes hydrogen bond and salt bridge contacts with *Mtb*-AnPRT via its carboxyl groups. Our results reveal how the substrate capture mechanism of AnPRT can be exploited to inhibit the enzyme's activity and provide a scaffold for the design of improved *Mtb*-AnPRT inhibitors that may ultimately form the basis of new antituberculosis drugs with a novel mode of action.



Tuberculosis (TB), the disease caused by the bacterium *Mycobacterium tuberculosis* (*Mtb*), continues to be a major global health burden in the 21st Century, with an estimated 2 billion people infected and almost 1.5 million deaths caused by TB in 2010.¹ Multidrug resistant (MDR) or extensively drug resistant (XDR) *Mtb* strains cause almost 4% of new TB cases² but are responsible for almost 9% of deaths from the disease. This is because they require treatment with second-line drugs that are less potent, have more side effects, and are much more expensive than the first-line antibiotics approved for *Mtb*. XDR-TB cases have now been confirmed in 58 countries, and the prevalence of these strains is increasing, making the development of new anti-TB agents a priority.

Genetic analysis has revealed a set of new potential drug targets in *Mtb*, including the biosynthetic pathways for a number of amino acids. For example, a genetic knockout in the tryptophan biosynthetic pathway [*trpD* or Rv2192c, the open reading frame encoding anthranilate phosphoribosyltransferase (AnPRT)] produced an auxotrophic *Mtb* strain that is essentially avirulent, even in immunodeficient mice,³ showing the essentiality of this pathway for pathogenesis. As mammals do

not synthesize tryptophan, the enzymes in this pathway therefore appear to be attractive potential targets for new anti-TB drugs.

AnPRT catalyzes the second step in the tryptophan biosynthesis pathway. In the reaction, 5'-phosphoribosyl 1'-pyrophosphate (PRPP) donates a phosphoribosyl group, which is added to the amino group of anthranilate to make N-(5'-phosphoribosyl)anthranilate (PRA) (Figure 1). The use of PRPP as a phosphoribosyl source is a general characteristic of phosphoribosyl transferases (PRTs), which require the presence of a divalent metal, usually magnesium, to catalyze transfer to their specific nitrogenous bases.^{4,5} The only specific AnPRT inhibitor recorded to date in the literature is 3-hydroxyanthranilate, with a reported K_i of 12 μM .⁶

AnPRT is the only representative of a type IV PRT and is structurally distinct from the other PRTs (types I–III).⁵ PRT type IV enzymes have the same fold as type II nucleoside phosphorylases (NP), the family of enzymes that catalyze the

Received: October 9, 2012

Revised: January 29, 2013

Published: January 30, 2013



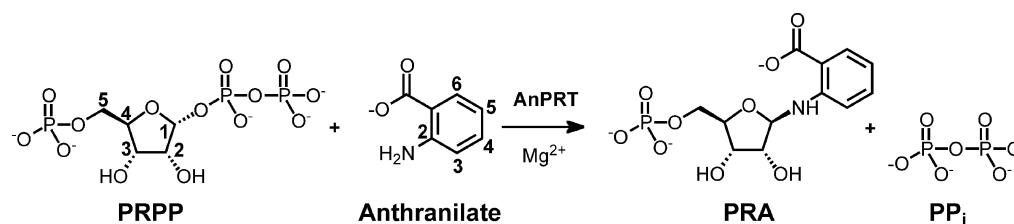


Figure 1. Reaction catalyzed by AnPRT.

removal of the ribosyl group from pyrimidines. Thus, AnPRT represents a link between two classes of enzyme, which catalyze near-reverse reactions.⁷ Interestingly, both type II NP enzymes and type I PRT enzymes undergo significant conformational changes upon substrate binding, and crystal structures of NPs and PRTs that are “closed” to various degrees have been observed. In type II NP enzymes, the conformational change involves rotation of the two domains relative to each other about the “hinge” region, whereas in PRT type I enzymes, it involves a flexible loop rearranging to effectively close the substrate-binding pocket. This suggests the importance of sequestering the highly reactive transition state or intermediate, which is proposed to have carbenium ion character in both reactions.^{8,9}

The structure of *Mtb*-AnPRT has previously been determined in both substrate-free and PRPP-bound forms [Protein Data Bank (PDB) entries 2BPQ and 1ZVW, respectively].¹⁰ AnPRT enzymes from other bacteria have also been characterized structurally, including those from *Sulfolobus solfataricus* (*Sso*),⁷ *Thermus thermophilus* (PDB entry 1V8G), *Nostoc* sp. (PDB entry 1VQU), and *Pectobacterium carotovorum* (*Pca*).¹¹ *Mtb*-AnPRT, like its homologues, forms an S-shaped homodimer, with each monomer consisting of an all-helical N-terminal domain and a larger α/β C-terminal domain, separated by a deep cleft.^{7,10,11} The N-terminal domain is composed of a four-helix bundle ($\alpha 1$ – $\alpha 4$, residues 1–89), decorated with two additional helices ($\alpha 8$ and $\alpha 9$, residues 189–209), and is joined to the C-terminal domain by three chain segments (between $\alpha 4$ and $\beta 1$, $\beta 3$ and $\alpha 8$, and $\alpha 9$ and $\beta 4$).¹⁰ Dimerization occurs solely through the N-terminal domain, via helices $\alpha 1$, $\alpha 3$, and $\alpha 8$.

The structure of *Mtb*-AnPRT soaked with PRPP (PDB entry 1ZVW) shows the substrate binding at the bottom of a deep cleft. The pyrophosphate of PRPP is coordinated to a Mg²⁺ ion and forms hydrogen bonds with residues from the N-termini of helices $\alpha 5$ and $\alpha 6$, and β -strands $\beta 1$ and $\beta 2$ from the C-terminal domain. The remainder of the PRPP molecule is bound by two loops that link these α -helices and β -strands ($\beta 1$ – $\alpha 5$, residues 107–117, loop I; $\beta 2$ – $\alpha 6$, residues 138–146, loop II) and close around the PRPP substrate on each side.^{7,10,11} Loop I contains a glycine-rich phosphate-binding sequence motif, and loop II contains an invariant asparagine, Asn138, which coordinates the hydroxyl groups of the ribose ring via its backbone carbonyl oxygen.¹⁰ A third substrate-binding loop has also been identified ($\beta 5$ – $\beta 6$, residues 247–258, loop III) and is involved in coordinating both Mg²⁺ ions that bind in association with PRPP.

Anthranilate binding to the *Mtb*-AnPRT–PRPP–Mg²⁺ complex (PDB entry 1ZVW) was modeled using GOLD,¹² which predicted two distinct binding sites.¹⁰ The first, which is presumably the catalytically relevant site, is adjacent to PRPP, with the anthranilate making contact with the side chain amide group of the invariant Asn138, as well as other residues located on the flexible PRPP-binding loops. The second predicted binding site is farther from the PRPP and near the entrance to the substrate-binding cleft. At this outer site, anthranilate makes a salt

bridge with a highly conserved arginine, Arg193, from the N-terminal domain. Similar “inner” and “outer” anthranilate binding sites were subsequently experimentally observed in the complex of *Sso*-AnPRT with PRPP and anthranilate (PDB entry 1ZKY).¹³ The sites were generally similar to those predicted for *Mtb*-AnPRT, with an anthranilate molecule at an inner site and another at an outer site, both of which make hydrogen bonds with the conserved asparagine from the flexible loop. Two histidines that are conserved in *Mtb*-AnPRT were also identified as π -acceptors with the potential to form weak hydrogen bonds with the C–H groups on the aromatic rings of anthranilate in both sites.¹³ To date, no other types of PRT have been observed to have two distinct binding modes for the same substrate within the active site pocket.

Here we report the first investigation into inhibition of *Mtb*-AnPRT and the first crystal structures of an AnPRT complexed with small molecule inhibitors. This provides insight into the binding modes of inhibitor molecules, supplies further evidence of the presence of two distinct anthranilate binding sites in *Mtb*-AnPRT, the outermost of which is proposed to have a role in substrate capture, and establishes a basis for the structure-based design of improved inhibitors.

EXPERIMENTAL PROCEDURES

Materials. Unless otherwise stated, all chemicals were obtained from Sigma-Aldrich, Scharlau, or Pure Science. All inhibitors characterized here were from Sigma-Aldrich except for ACS165 {hexanoic acid, 3-amino-6-[(2,4-dinitrophenyl)amino]-(6Cl)}, which was from BDH Chemicals.

Cloning, Expression, and Purification. The *Mtb trpD* gene had previously been cloned into expression vector pET23a, which adds a C-terminal His₆ tag.¹⁰ This plasmid was used to transform *Escherichia coli* BL21 (DE3) (Stratagene) and the same strain containing pRIL for expression of rare codons (Novagen), or plasmids (pBB528 and pBB541) for coexpression of chaperonins (GroES–GroEL).¹⁴ Use of the latter strain resulted in an improved soluble protein yield. Cells were grown in shaking flasks at 37 °C until the culture reached an OD₆₀₀ of 0.6. Expression of *Mtb*-AnPRT was induced by the addition of 1 mM isopropyl β -D-thiogalactopyranoside (IPTG), and the cells were incubated at 18 °C overnight, before being pelleted and frozen at –20 °C. For expression of selenomethionine (SeMet)-labeled *Mtb*-AnPRT, *E. coli* BL21 (DE3) pRIL cells harboring the *trpD* plasmid were grown in minimal medium at 37 °C to an OD₆₀₀ of >0.3. Cultures were then cooled to 18 °C and supplemented with branched chain amino acids and L-SeMet. Expression of *Mtb*-AnPRT was induced 30 min later with IPTG and growth continued overnight.¹⁵

Bacterial cell pellets were defrosted as needed, resuspended in lysis buffer [50 mM Tris–HCl (pH 8.0), 150 mM NaCl, and 10 mM imidazole], and lysed by being passed through a cell disrupter (Constant Systems Ltd.) at 2 kbar. *Mtb*-AnPRT was purified to homogeneity using affinity and gel filtration

chromatography as previously described,¹⁰ concentrated using a centrifugal concentrator (Vivaspin, 10000 molecular weight cutoff), and flash-cooled in liquid nitrogen before being stored at -80°C . The final storage buffer for AnPRT consisted of 50 mM Tris-HCl, 150 mM NaCl, 5 mM β -mercaptoethanol, and 5% (v/v) glycerol for crystallography and 50 mM KH_2PO_4 , 200 mM NaCl, and 25 mM imidazole for biochemical assays.

Biochemical Assays. The initial screen was performed in a 96-well plate using the fluorescence-based assay previously described.¹⁰ An enzyme-coupled absorbance-based assay developed in house was used to determine the inhibitor–enzyme kinetic parameters of *Mtb*-AnPRT, including K_i values for the inhibitors. Conversion of PRA, the product of *Mtb*-AnPRT, by PRA isomerase-indoleglycerol phosphate synthase (PRAI-InGPS) into indoleglycerol phosphate (InGP) can be monitored spectrophotometrically at 270 nm.¹⁶ PRAI-InGPS was added in excess to ensure that the AnPRT-catalyzed reaction is the rate-limiting step and to prevent feedback inhibition caused by the buildup of PRA. The extinction coefficient for InGP production from anthranilate and PRPP was determined to be $7500\text{ L mol}^{-1}\text{ cm}^{-1}$ at 270 nm under assay conditions that included known concentrations of anthranilate.

All assays were conducted with a Varian Cary 100 UV–vis spectrophotometer using quartz cuvettes thermally equilibrated to 25°C . The final concentrations of the following components were included in the coupled assay: PRPP (0.6 mM), MgCl_2 (1 mM), *Mtb*-AnPRT (0.1 μM), *Eco*-PRAI-InGPS (1.7 μM), anthranilate (0–140 μM), inhibitor (0–150 μM), and Tris-HCl buffer [50 mM Tris and 150 mM NaCl (pH 8.0)]. The Tris buffer solution was made using ultrapure water that had been pretreated with Chelex, and all other solutions were subsequently made using this Tris buffer. Reactions were initiated via the addition of *Mtb*-AnPRT, with initial rates of reaction determined by a least-squares fit of the initial rate data and the average value of two replicates used for subsequent K_i determination. K_i values were obtained by fitting the data to the Michaelis–Menten equation using GraFit 5 (Erithacus Software).¹⁷

Crystallization. Prior to crystallization, aliquots of *Mtb*-AnPRT at 3–6.6 mg/mL were thawed by incubation at 37°C and where applicable mixed with 10 mM PRPP, 10 mM MgCl_2 , and 1–5 mM inhibitor (dissolved in DMSO). High-quality crystals of *Mtb*-AnPRT in complex with inhibitors were obtained in hanging drops of 1 μL of protein solution [in 50 mM Tris-HCl, 150 mM NaCl, 5 mM β -mercaptoethanol, and 5% (v/v) glycerol] with 1 μL of reservoir solution. Initially, crystals of *Mtb*-AnPRT in complex with PRPP, Mg^{2+} , and inhibitors were grown in 24-well screens of 0.2 M cacodylate (pH 5.5–7.0) and 6–12% PEG6000, based on the condition identified by Lee et al.¹⁰ but without the additive benzamidine. Selenomethionine-labeled *Mtb*-AnPRT was used as this had crystallized more readily than the native form in previous work.

New conditions for crystallization of native *Mtb*-AnPRT in the absence of benzamidine [0.2 M imidazole/malate (pH 8.0) and 15% PEG4000] were found by sitting-drop vapor diffusion (0.1 μL of protein solution with 0.1 μL of precipitant) in IntelliPlate plates (Art Robbins Instruments) at 291 K using a Cartesian Honeybee dispensing robot with an in-house 480-component screen.¹⁸ Optimized crystals of *Mtb*-AnPRT, in its substrate-free form and in complex with PRPP, Mg^{2+} , and various inhibitors, were obtained in 24-well screens of 0.2 M imidazole/malate (pH 7.0–8.5) and 10–20% PEG4000. For inhibitors for which high-quality crystals were not obtained using this method, the screen was repeated and crystallization drops were seeded from native

substrate-free crystals using a cat whisker. Precise crystallization conditions for each inhibitor are listed in Table S3 of the Supporting Information. The crystals generally had block morphology and grew to dimensions of $\sim 0.1\text{ mm} \times 0.8\text{ mm} \times 0.5\text{ mm}$ within 2 weeks.

For data collection, crystals were removed from the crystallization drop with a nylon loop. The cocrystallized *Mtb*-AnPRT–inhibitor crystals were soaked in a cryoprotectant containing the mother liquor and 26% glycerol before being flash-cooled in liquid nitrogen.

Data Collection, Structure Solution, and Refinement.

Data were collected at the Australian Synchrotron, beamline MX2, and on the home source. The crystals of the *Mtb*-AnPRT–inhibitor complexes diffracted to a maximum resolution that varied between 1.6 and 2.4 Å. X-ray diffraction data were indexed, integrated, and scaled with the autoPROC suite,¹⁹ XDS,²⁰ and SCALA²¹ or with the HKL2000 suite of programs.²² Chain A of the original *Mtb*-AnPRT–PRPP complex structure (PDB entry 1ZVW),¹⁰ without ligands, was used as the search model for structure determination by molecular replacement using MOLREP,²³ and as the initial model for refinement of the AnPRT–inhibitor complex structures. Refinement and model building were performed with Coot²⁴ and Refmac5,²⁵ or autoBUSTER,²⁶ with restraints for the inhibitors generated by using the PRODRG server.²⁷ Restraints on bond lengths and angles were based on the ideal values of Engh and Huber,²⁸ and model quality was assessed using MolProbity.²⁹ Full data collection and refinement statistics are listed in Table 2. Figures illustrating structural details were prepared using PyMOL,³⁰ with maps generated with FFT³¹ in the CCP4 suite,³² and the inhibitor binding modes were characterized using LigPlot+.³³ Structural superpositions were performed with SSM,³⁴ using the C α atoms of residues 25–369 for comparing monomers of *Mtb*-AnPRT and the C α atoms of secondary structure elements for comparing monomers of *Mtb*-AnPRT and *Sso*-AnPRT.

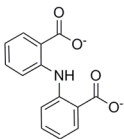
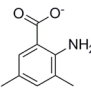
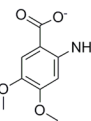
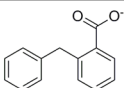
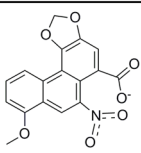
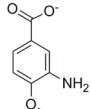
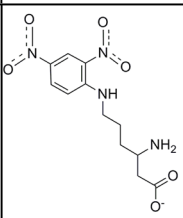
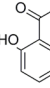
The crystallographic coordinates and structure factor amplitudes for all structures have been deposited in the Protein Data Bank with the entries listed in Table 1.

RESULTS AND DISCUSSION

Compounds of Anthranilate and Bianthranilate Character Inhibit *Mtb*-AnPRT. To identify inhibitors of *Mtb*-AnPRT, a targeted library of 165 compounds from the Auckland Cancer Society Research Centre (ACSRC) was screened (Figure S1 of the Supporting Information) using the fluorescence assay originally developed by Bauerle et al.³⁵ The compounds were chosen from the ACSRC in-house chemical collection, based on their substratelike or metal binding properties. The best inhibitory compounds were found to have aromatic rings with a carboxyl group, and most had substituents at position 2, like the native substrate anthranilate (Figure 1). A number of these compounds (e.g., ACS125 and ACS130) were competent to undergo the phosphoribosyl transferase reaction catalyzed by *Mtb*-AnPRT to form PRA derivative products. These will be discussed elsewhere (manuscript in preparation). In the study presented here, we focus on the compounds that did not act as alternative substrates (Table 1), with the aim of structure-based inhibitor design.

The inhibition properties of the top compounds from the screen were characterized using an absorbance assay that coupled AnPRT activity with the subsequent enzyme in the tryptophan pathway, PRA isomerase-indoleglycerol phosphate synthase. The use of an absorbance assay prevented interference from

Table 1. Chemical Structures, K_i Values, and PDB Entries of Inhibitors

ACS No.	Structure	K_i (μ M)	PDB ID	Resolution (\AA)	Binding modes
172		1.5 ± 0.1	3QQS	1.97	2 ^a
142		6.3 ± 0.8	3UU1	1.82	2
145		15 ± 4	3R88	1.73	1
174		18 ± 2	3QS8	2.15	2
179		19 ± 5	3R6C	1.83	1 ^b
126		60 ± 13	n/a ^c	n/a	n/a
165		79 ± 17	n/a	n/a	n/a
10		119 ± 20	3TWP	1.83	1

^aThere is a third binding mode that involves contacts between different dimers and, hence, is likely an artifact of crystal packing.

^bThere is a second mode in a hydrophobic region on the surface of the protein that is likely a crystallographic artifact. ^cNot available.

inhibitors that fluoresced at wavelengths similar to that of anthranilate. Inhibition constants (K_i) were determined by fitting a competitive inhibition model with respect to anthranilate (Figure S2 of the Supporting Information) and ranged from 1.5 to 119 μ M (Table 1). The strongest inhibition ($K_i = 1.5 \pm 0.1 \mu$ M) was observed for compound ACS172 [2-(2-carboxyphenylamino)benzoic acid], which is composed of two benzoic acid rings linked via a secondary amine and is thus bianthranilate-like in character.

A New Crystallization Protocol Reveals More of the Active Site Pocket of *Mtb*-AnPRT. A new substrate-free structure of *Mtb*-AnPRT was determined in the process of optimizing the crystallization protocol for inhibition studies (PDB entry 3QR9). A new crystallization condition was found [0.2 M imidazole/malate (pH 8.0) with 15% PEG4000 as a precipitant] that produced crystals that diffracted to 1.87 \AA , without the need for the addition of benzamidine, which had previously been required to produce diffraction-quality crystals.¹⁰ This new substrate-free structure, although largely similar to that reported previously, showed two significant differences: helix $\alpha 8$ of the N-terminal domain is shifted by $\sim 5 \text{\AA}$, narrowing the entrance to the active site, and loop II no longer folds into the substrate-binding cleft (Figure 2).

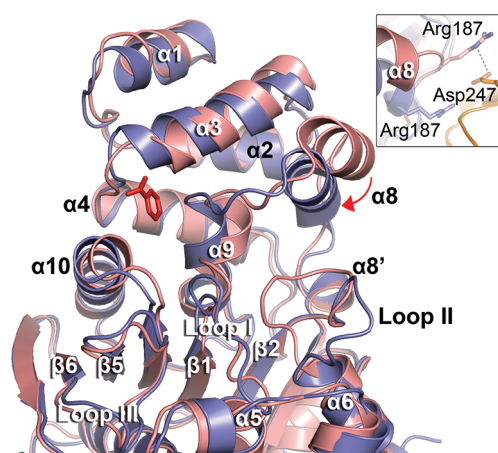


Figure 2. New substrate-free structure of *Mtb*-AnPRT. The new substrate-free crystal structure of *Mtb*-AnPRT (PDB entry 3QR9, chain A, blue) is shown superimposed on the original substrate-free structure (PDB entry 2BPQ, chain A, pink), which was cocrystallized with benzamidine (red). The inset shows the movement of helix $\alpha 8$ and the reorientation of Arg187, which forms a salt bridge with Asp247 from an adjacent molecule in the crystal (orange) in the original substrate-free structure.

We propose that helix $\alpha 8$ in the original substrate-free (PDB entry 2BPQ) and PRPP-bound (PDB entry 1ZVW) structures of *Mtb*-AnPRT was captured in a conformation favored by the crystal packing in the original crystal form. Superposition of the new substrate-free structure on the original substrate-free structure of *Mtb*-AnPRT shows that the latter has several α -helices ($\alpha 3$, $\alpha 9$, and $\alpha 10$) that appear to have rearranged around the benzamidine binding site, with these movements propagating outward to helix $\alpha 8$ (Figure 2). Helix $\alpha 8$ is longer in the new ligand-free structure and includes Arg187, which in the original structure formed a salt bridge with Asp247 from an adjacent molecule as part of a crystal contact (Figure 2, inset). In addition, the length of helix $\alpha 8$ and its position adjacent to the substrate entrance in the new substrate-free *Mtb*-AnPRT structure are consistent with the substrate-free structures of AnPRT from other bacterial species (PDB entries 1KHD, 1O17, 1V8G, and 2ELC).^{7,11} Taken together, these observations suggest that the position of helix $\alpha 8$ in the original structures (PDB entries 2BPQ and 1ZVW) arises from the presence of the crystallization additive or from crystal packing.

The different positions of loop II in the two substrate-free structures of *Mtb*-AnPRT reflect the inherent flexibility of this loop, which is important for substrate binding. Both loops I and

Table 2. Data and Refinement Statistics for All Complexes

	AnPRT	AnPRT–PRPP–ACS172	AnPRT–PRPP–ACS142	AnPRT–PRPP–ACS145
	Data Collection			
space group	$P2_12_12_1$	$P2_1$	$P2_1$	$C2$
cell dimensions				
a, b, c (Å)	79.5, 91.8, 120.1	94.9, 78.2, 101.7	78.2, 111.0, 80.4	94.3, 78.9, 100.5
β (deg)	90.0	111.0	89.97	110.3
no. of unique reflections	72847	97403	116249	71917
resolution range ^a (Å)	26.5–1.86 (1.96–1.86)	94.9–1.97 (2.08–1.97)	111.0–1.82 (1.92–1.82)	94.3–1.73 (1.82–1.73)
$R_{\text{merge}}^{a,b}$	0.079 (0.74)	0.091 (0.72)	0.076 (0.48)	0.065 (0.66)
$I/\sigma(I)^a$	19.4 (2.6)	11.9 (2.0)	11.1 (3.0)	23.1 (3.3)
completeness ^a (%)	98.1 (87.6)	99.1 (97.8)	95.2 (73.5)	99.8 (99.2)
redundancy ^a	6.9 (6.7)	3.7 (3.6)	4.6 (3.4)	7.3 (7.0)
Wilson B factor (Å)	23.8	23.3	17.9	20.3
	Refinement			
resolution range (Å)	26.5–1.87	94.9–1.97	80.4–1.82	58.9–1.73
no. of atoms, B factor ^c				
protein	5006, 23.9	9898, 26.1	9813, 19.8	4976, 19.4
solvent	520, 32.4	601, 30.2	1087, 30.4	689, 33.4
$R_{\text{work}}^{a,d}$ (%), $R_{\text{free}}^{a,e}$ (%)	18.7, 21.4 (32.9, 35.7)	21.6, 25.9 (29.1, 32.6)	21.2, 25.6 (65.6, 69.8)	17.5, 21.4 (24.9, 29.2)
Ramachandran outliers ^f (%)	0.3	0.4	0.3	0.3
rmsd ^g				
bond lengths (Å)	0.015	0.012	0.014	0.011
bond angles (deg)	1.46	1.46	1.45	1.42
	AnPRT–PRPP–ACS174	AnPRT–PRPP–ACS179	AnPRT–PRPP–ACS10	
	Data Collection			
space group	$P2_1$	$C2$	$P2_1$	
cell dimensions				
a, b, c (Å)	78.4, 80.8, 110.5	94.0, 77.9, 99.8	78.7, 111.3, 81.1	
β (deg)	90.0	110.2	90.1	
no. of unique reflections	94047	58097	104098	
resolution range ^a (Å)	110–2.15 (2.25–2.15)	93.7–1.83 (1.93–1.83)	111.3–1.83 (1.93–1.83)	
$R_{\text{merge}}^{a,b}$	0.068 (0.64)	0.055 (0.37)	0.044 (0.24)	
$I/\sigma(I)^a$	19.8 (2.2)	24.8 (5.2)	15.3 (4.4)	
completeness ^a (%)	98.8 (98.9)	98.0 (86.0)	96.4 (76.8)	
redundancy ^a	7.4 (6.3)	7.1 (5.7)	3.6 (2.9)	
Wilson B factor (Å)	23.7	19.5	18.2	
	Refinement			
resolution range (Å)	110.4–2.15	93.7–1.83	81.1–1.83	
no. of atoms, B factor ^c				
protein	10020, 23.6	5010, 21.3	10003, 19.4	
solvent	829, 33.8	572, 32.5	1199, 30.7	
$R_{\text{work}}^{a,d}$ (%), $R_{\text{free}}^{a,e}$ (%)	17.7, 21.4 (22.4, 28.1)	18.6, 22.7 (51.7, 53.1)	19.3, 23.8 (53.9, 56.9)	
Ramachandran outliers ^f (%)	0.3	0.3	0.3	
rmsd ^g				
bond lengths (Å)	0.014	0.009	0.013	
bond angles (deg)	1.49	1.50	1.43	

^aData for the outer resolution shell are given in parentheses. ^b $R_{\text{merge}} = \sum_{hkl} I(hkl) - \langle I(hkl) \rangle / \sum_{hkl} I(hkl)$, where $\langle I(hkl) \rangle$ is the mean of the symmetry-equivalent reflections of $I(hkl)$. ^c \bar{A}^2 The average atomic temperature factor. Details of the average atomic temperature factors for the ligands in the structures are given in Table S2 of the Supporting Information. ^d $R_{\text{work}} = \|F_o\| - \|F_c\| / \|F_o\|$. ^e $R_{\text{free}} = \sum_T \|F_o\| - \|F_c\| / \sum_T \|F_o\|$ (where T is a test data set of 5% of the total reflections randomly chosen and set aside before refinement). ^fRamachandran outliers calculated using Molprobity.²⁹ ^gIdeal values from Engh and Huber.²⁸

II are involved in binding PRPP, and without PRPP, the residues from these loops are disordered (either lacking electron density or with high B factors) in both the new substrate-free *Mtb*-AnPRT crystal structure (PDB entry 3QR9) and in all other substrate-free AnPRT structures (PDB entries 2BPQ, 1KHD, 1O17, 1V8G, and 2ELC).^{7,11} Structural alignment of the new substrate-free structure with an *Mtb*-AnPRT–inhibitor–PRPP complex structure (Figure S3 of the Supporting Information) shows that both loops I and II move significantly upon substrate

binding. This suggests that *Mtb*-AnPRT, in a manner analogous to that of the structurally dissimilar PRT type I enzymes, protects its highly reactive carbenium ion intermediate from solvent by rearrangement of flexible loops.

The movement of loops I and II upon PRPP binding, along with the new position of helix $\alpha 8$, results in an ~ 15 Å long tunnel between the PRPP and the solvent, which contains both predicted anthranilate binding sites. The position of helix $\alpha 8$ affects the predicted binding of anthranilate in the outer site as it

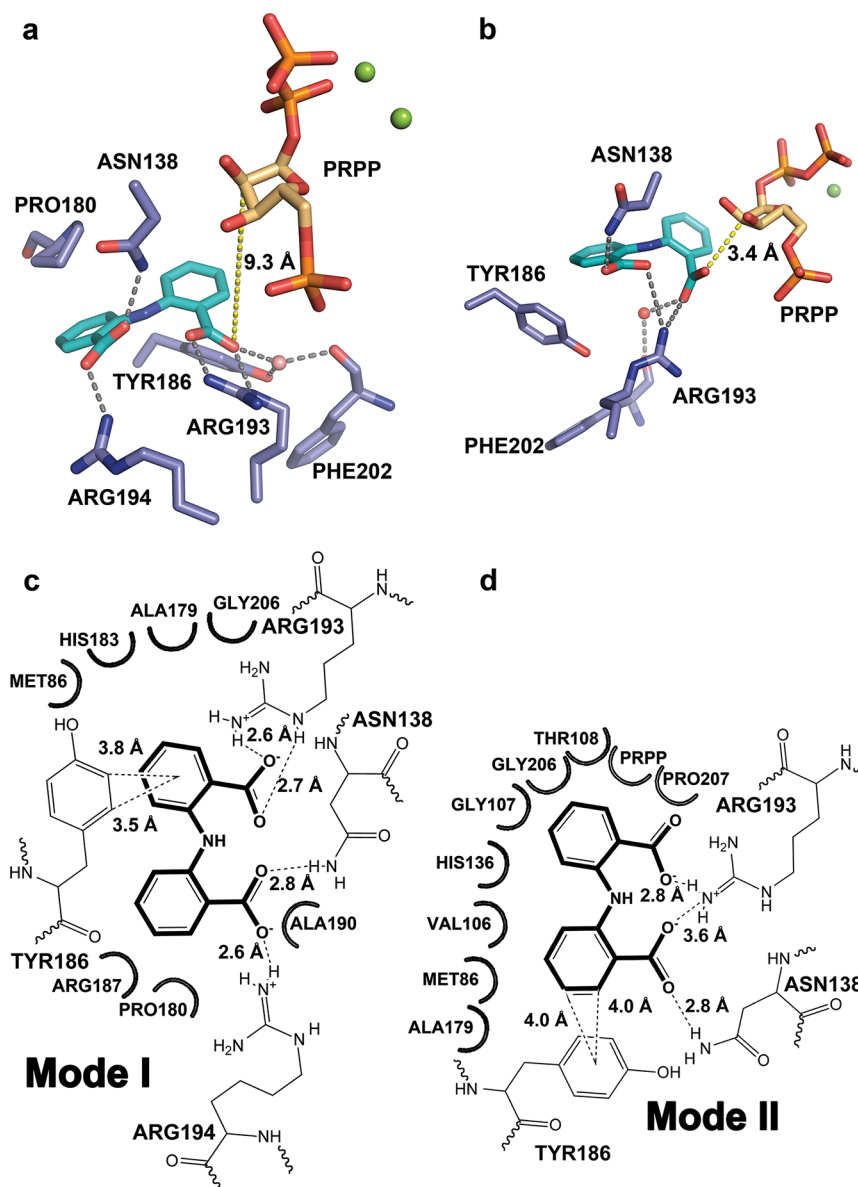


Figure 3. Two binding modes observed for inhibitor ACS172. (a) ACS172 binding in mode I and (b) ACS172 binding in mode II. The distance from the inhibitor carboxylate oxygen to C2 of PRPP is shown as a yellow dashed line in each case. Hydrogen bonds and salt bridges between the inhibitor and the protein are shown as gray dashed lines. (c and d) Schematic representations of the two ligand binding modes. Residues within 4 Å of the inhibitor are shown as semicircles to represent van der Waals interactions.

brings extra residues into the interdomain cleft, such that they are able to interact with incoming molecules. Thus, the new crystallization protocol was important for determining and analyzing the binding mode of the inhibitor compounds as discussed below.

Binding of the Most Potent Inhibitor, ACS172. Because *Mtb*-AnPRT was predicted to have two adjacent anthranilate binding sites,^{10,13} and the most potent inhibitor identified in our screen (ACS172) is bianthranilate-like in character, it was important to determine the exact mode of binding of this inhibitor to the enzyme. To elucidate its binding mode, inhibitor ACS172 was cocrystallized with *Mtb*-AnPRT. The cocrystals formed in space group $P2_1$, with four monomers per asymmetric unit, corresponding to two homodimers of *Mtb*-AnPRT. The structure was determined by molecular replacement using chain A of the original *Mtb*-AnPRT–PRPP complex structure (PDB entry 1ZVW),¹⁰ with the ligands removed, as the search model. It

was then refined against data to a resolution of 1.97 Å, with excellent refinement statistics and geometrical parameters (Table 2).

Clear electron density in one of the subunits of each homodimer (corresponding to chains A and B) allowed for unambiguous placing of the inhibitor at full occupancy (Figure 3a and Figure S4a of the Supporting Information). The positions of PRPP and two Mg^{2+} ions were also clearly identified, but the ribosyl ring of PRPP showed evidence of multiple conformations, as has been observed previously in other AnPRT enzymes,^{7,13} and was refined with an occupancy of 0.5. As mentioned above, the associated PRPP-binding loops adopted a “closed” conformation compared to the substrate-free structure (Figure S3 of the Supporting Information). In this subunit, ACS172 binds in a site that overlaps with the outer anthranilate binding site (Figure 4a), with the carboxylic acid group of the inhibitor 9.3 Å from C2 of PRPP (Figure 3a). This binding mode, termed

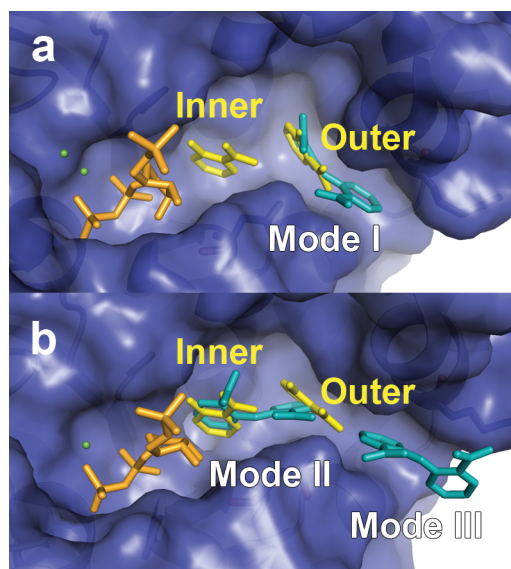


Figure 4. Position of the most potent inhibitor in the substrate-binding tunnel. The cocrystal structure of *Mtb*-AnPRT, inhibitor ACS172, PRPP, and Mg^{2+} (PDB entry 3QQS) is superimposed on the *Sso*-AnPRT crystal structure (PDB entry 1ZYK) determined by Marino et al.¹³ (a) Binding mode I of ACS172 (cyan) overlaps with the outer binding site of anthranilate (yellow) observed in the *Sso*-AnPRT crystal structure. (b) Binding mode II of ACS172 (cyan) overlaps with both the inner and outer binding sites of anthranilate (yellow) observed in *Sso*-AnPRT.

mode I, is formed by residues from helix $\alpha 8$, loop II, and a region linking the C-terminal and N-terminal domains ($\alpha 8$ – $\beta 3$) (Figure S4a of the Supporting Information), thus occupying the outer end of the substrate-binding tunnel formed by helix $\alpha 8$. The carboxylic acid groups of ACS172 form salt bridges with the guanidinium groups of Arg193 and Arg194 from helix $\alpha 8$, and hydrogen bonds are made with the side chain amide group of Asn138 from loop II and the backbone carbonyl oxygen of Phe202 via an ordered water (Figure 3a,c). The plane of the outermost ring of ACS172 is stacked parallel with that of Pro180 (Figure 3a), with 3.9 Å between the two rings (Figure 3c), suggestive of possible weak hydrogen bonds between the hydrogens of the proline ring and the π -electron cloud of the aromatic ring of ACS172.³⁶ The inner ring of ACS172 packs in a plane-to-edge fashion against the phenyl ring of Tyr186, and the distances again suggest possible C–H $\cdots\pi$ interactions^{37,38} between Tyr186 and the ACS172 aromatic ring.

In the other subunit of each homodimer (corresponding to chains C and D), a different binding mode for ACS172 was observed, with the inhibitor bound such that its carboxylic acid group is only 3.4 Å from C2 of PRPP (Figure 3b). In this binding mode, termed mode II, the ACS172 molecules had a lower occupancy (0.6), suggesting that this is a less favored binding mode in the crystal structure (Figure S4c of the Supporting Information) and the electron density was less clear for PRPP (and for the associated PRPP-binding loops) in this subunit, with little visible density for the ribosyl moiety, indicating that in addition to the ribose ring, the entire PRPP molecule has increased flexibility (Figure S4c of the Supporting Information). In mode II, the outer ring of the inhibitor packs in plane-to-edge fashion against the phenyl ring of Tyr186 (Figure 3b,d), with its carboxylic acid hydrogen bonded to Asn138 and the inner ring occupying part of the predicted inner anthranilate site (Figure 4b). In this subunit, a second ACS172 molecule was also

observed near the entrance to the substrate-binding tunnel (Figure 4b). However as this outermost site (mode III binding) also involves crystal contacts (Figure S5 of the Supporting Information), it was presumed to not represent a likely binding mode in solution and thus is not described in detail. Although we cannot rule out the possibility that mode II binding is also favored or even driven by crystal packing, the fact that it mimics some substrate-like contacts makes it a useful guide for the design of improved inhibitors.

The significance of binding mode II of ACS172 is that it directly prevents anthranilate from binding to its catalytically relevant binding site. Although mode I binding does not overlap with the catalytically relevant anthranilate binding site, it involves several residues from both domains of the protein, and binding here would block incoming molecules from entering the enzyme active site via the substrate-binding tunnel (Figure 4a). Hence, binding in either site could contribute to enzyme inhibition. In addition, having two possible binding modes, corresponding to slightly different conformations of the residues in the binding pocket, may contribute to the overall potency of the bianthranilate inhibitor against *Mtb*-AnPRT.

The Substrate-Binding Tunnel Entrance Binds Chemically Diverse Inhibitors. Following the observation that ACS172 binds at the entrance to the substrate-binding tunnel, an additional five of the best inhibitors identified from the initial screen (ACS10, ACS142, ACS145, ACS174, and ACS179) were cocrystallized with *Mtb*-AnPRT and their binding sites examined. Attempts to cocrystallize *Mtb*-AnPRT with inhibitors ACS126 and ACS165 were unsuccessful, perhaps because of their higher K_i values of 60–70 μ M. The inhibitors that were observed in complex with the enzyme are diverse in structure, with some single-ring anthranilate mimics and some extended molecules containing multiple aromatic rings and side groups. All of these inhibitors could be observed in complex with *Mtb*-AnPRT, from cocrystal structures determined at resolutions ranging from 1.8 to 2.4 Å (Tables 1 and 2, Figure 5, and Figure S6 of the Supporting Information).

The binding mode of these inhibitors broadly matched binding mode I of ACS172, with variations in the number and location of hydrogen-bonded contacts (Figure 5). Binding in the outer anthranilate-binding site is the only mode of binding observed for ACS145, ACS179, and ACS10, whereas other compounds also bind in the inner anthranilate-binding site (Table 3, discussed below). Some residues were universally involved in binding at the outer site, whereas others appear to be dispensable, while still contributing additional interactions for some inhibitors (Table 3). Hydrophobic interactions and/or π -interactions with Pro180 and Tyr186 on either side of the aromatic plane were universal, and this “hydrophobic sandwich” appears to be the main determinant of binding at the outer site. Residues Asn138 and Arg193 also appeared to be fundamental for binding here, as all of the inhibitors were observed to form hydrogen bonds with one or both of these residues. The cocrystal structures of the other inhibitors binding to this site were very similar to the cocrystal structure of ACS172, as reflected by small rmsds when the monomer structures were overlaid (0.35 Å for ACS142, 0.43 Å for ACS145, 0.29 Å for ACS174, 0.25 Å for ACS179, and 0.33 Å for ACS10).

Molecules binding at the outer anthranilate site at the entrance to the substrate-binding tunnel are presumed to prevent enzyme activity by blocking anthranilate from reaching the catalytic site deeper inside the enzyme. Although it is conceivable that anthranilate could enter the active site without first passing

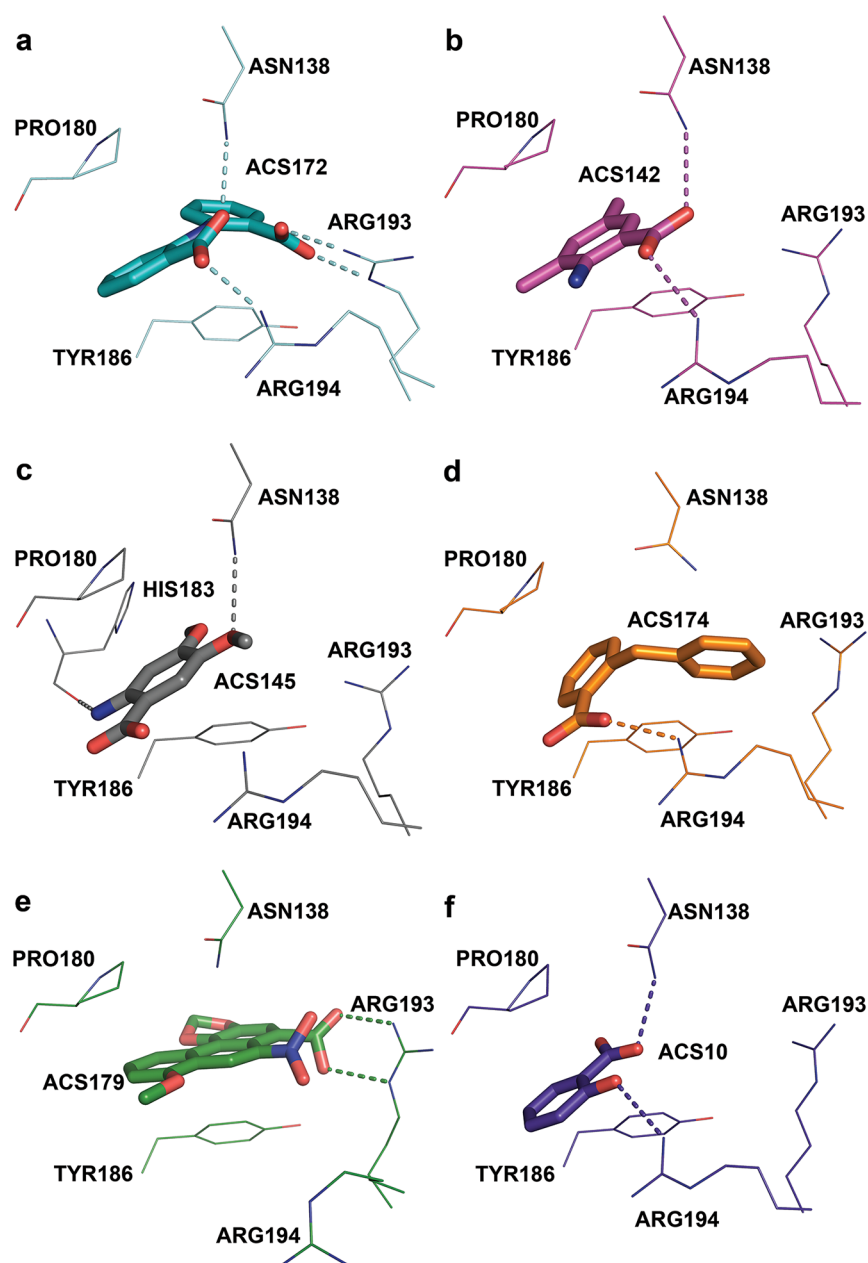


Figure 5. Inhibitors binding at the substrate tunnel entrance. (a) Binding mode I of ACS172 (PDB entry 3QQS, chain A, cyan) in comparison to the binding modes of (b) ACS142 (PDB entry 3UU1, chain A, pink), (c) ACS145 (PDB entry 3R88, chain B, gray), (d) ACS174 (PDB entry 3QS8, chain A, orange), (e) ACS179 (PDB entry 3R6C, chain A, green), and (f) ACS10 (PDB entry 3TWP, chain A, purple) in the cocrystal structures of *Mtb*-AnPRT, PRPP, and Mg^{2+} with the various inhibitors.

through the substrate-binding tunnel, it would require rearrangement of the PRPP-binding loops. However, most of the inhibitors, like ACS172, form hydrogen bonds with residue Asn138, which is located on one of the flexible PRPP-binding loops, suggesting that inhibitor binding could stabilize the flexible loop in the “closed” conformation, effectively preventing both the exchange of PRPP and any potential simultaneous binding of anthranilate.

Several of the inhibitors tested were composed of single aromatic rings with varying substituents (ACS10, ACS142, and ACS145). It is perhaps surprising a priori that these single-aromatic ring inhibitors were observed to bind preferentially at an outer binding site rather than at the catalytic site. However, this preference was observed for ACS145 both when it was cocrystallized with *Mtb*-AnPRT and in soaking experiments

(data not shown) and provides further evidence that the outer site, previously observed in docking experiments and crystal structures of *Sso*-AnPRT, is functionally relevant, presumably for substrate capture, in bacterial AnPRTs.

Assuming the binding modes observed crystallographically are also the relevant modes in solution, this information together with the kinetic analysis of these inhibitors suggests that relatively strong inhibition can be obtained by blocking the substrate-binding tunnel entrance.

Inhibitor Binding at Multiple Sites in the Substrate-Binding Tunnel. Two moderately potent inhibitors, ACS174 ($K_i = 18 \pm 2 \mu M$) and ACS142 ($K_i = 6.3 \mu M$), showed additional binding interactions distinct from the hydrophobic sandwich at the substrate-binding tunnel entrance seen in the other inhibitor cocrystal structures.

Table 3. List of Contacts Made by Inhibitors^a

inhibitor	ACS172		ACS142		ACS145	ACS174		ACS179	ACS10
	outer	inner ^b	outer ^c	inner ^c	outer	inner ^d	outer ^d	outer	outer
	mode I	mode II							
PRPP		+	++	++		+	+		
Met86	+	+				+		++	
Val106		+				+		+	
Gly107		+				+			
Thr108		+							
His136		+		+				+	
Gly137		+		+					
Asn138	+++	+++	+++	+	+++	+	+	+	+++
Arg139								++	
Ala141							+		
Ala179	+	+	+	+	+	+	+	+	+
Pro180	+		+		+		+	+	+
His183	+		+	+	+++		+	+	+
Pro184			+						
Tyr186	++	+	+		+	+++		+++	+
Arg187	+		+		++		++		+
Ala190	+		+		+		+	+	+
Arg193	+++	+++		+++		+++		+++	
Arg194	+++		+++		++		+++		+++
Ala197									
Phe202	++	++				+			
Asn203						++		++	
Leu205						+		+	
Gly206	+	++		+		++		++	
Pro207		+							
Thr209				+		+		+	

^aContacts were initially identified by LigPlot+, where hydrogen bonds are defined by spatial (<3.3 Å) and geometric parameters.³³ The symbols correspond to the type of interaction: +, van der Waals interactions or π -interactions (<4.0 Å); ++, water-mediated hydrogen bonds; +++, hydrogen bonds or salt bridges. Both inner modes involved the binding of another inhibitor molecule in the outer position. The data are bold if the equivalent residue was identified as being part of the anthranilate binding sites in the *Sso*-AnPRT structure (PDB entry 1ZYK) determined by Marino et al.¹³

^bThis mode occurs simultaneously with binding mode III, with the inhibitors in hydrophobic contact with each other. Binding mode III involves contacts between different dimers and hence is not included. ^cThese modes occur simultaneously, with the inhibitors in hydrophobic contact with each other. ^dThese modes can occur simultaneously with the inhibitors in hydrophobic contact with each other or if only the inner motif is observed.

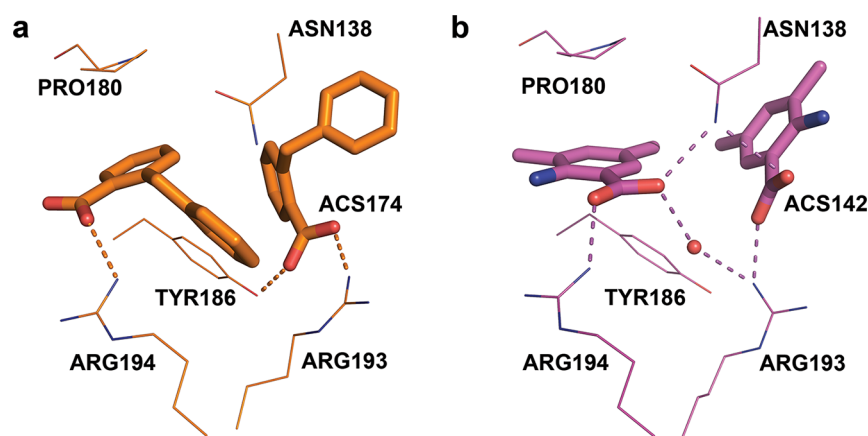


Figure 6. Alternative binding modes observed for ACS174 and ACS142. (a) Dual binding mode of ACS174 cocrystallized with *Mtb*-AnPRT, PRPP, and Mg²⁺ (PDB entry 3QS8). (b) Dual binding mode of ACS142 cocrystallized with *Mtb*-AnPRT, PRPP, and Mg²⁺ (PDB entry 3UU1).

ACS174 has a two-ring structure similar to that of ACS172 but contains a methylene group linking the rings in place of a secondary amine group, and the carboxylic acid substituent is present on only one of the two rings. The complex of *Mtb*-AnPRT with ACS174 and PRPP crystallized in the same space

group as the ACS172 complex, with four monomers per asymmetric unit corresponding to two homodimers of *Mtb*-AnPRT. Clear electron density allowed the unambiguous placement of both the inhibitor and PRPP (Figure 6 and Figure S4e of the Supporting Information), with the inhibitor again

displaying different binding modes for each subunit of the dimer, in the same manner as ACS172.

In all of the subunits of the cocrystal structure of *Mtb*-AnPRT, ACS174, PRPP, and Mg^{2+} , the inhibitor is bound with its benzoate ring in the site approximately equivalent to the inner ring of ACS172 in binding mode I (Figure 5d). In this position, the carboxylate group of ACS174 hydrogen bonds to Arg193 and Tyr186 and the benzene ring of ACS174 extends more deeply into the active site. In two of the four protein monomers in the asymmetric unit, an additional ACS174 molecule is also bound with its benzoate ring held by hydrophobic contacts to Arg194, Tyr186, and Pro180 and a hydrogen bond to Arg194 (Figure 6a). In this position, the benzene ring of the inhibitor extends sideways across the substrate-binding tunnel entrance, so that its center is only 3.9 Å from Arg194, possibly indicating an amino–aromatic hydrogen bond.³⁹ Interestingly, it seems that the benzoate rings of ACS174 recapitulate the binding of ACS172 in binding mode I (Figure 5a), but with the interactions split across two inhibitor molecules, perhaps explaining its weaker inhibition with a K_i of $18 \pm 2 \mu M$, compared to the value of $1.5 \pm 0.1 \mu M$ for ACS172.

Although most single-ring inhibitors were found to bind only to the site at the entrance to the substrate-binding tunnel, ACS142 bound simultaneously at two sites: with full occupancy at the outer site and at lower occupancy (~ 0.80) at an inner site (Figure 6b). ACS142 was also the best inhibitor of the smaller, single-ring compounds ($K_i = 6.3 \mu M$), and the second most potent of all the compounds tested, possibly reflecting its ability to bind at two sites. Density for the PRPP in this structure was incomplete (Figure S4e,f of the Supporting Information), raising the possibility that PRPP could have been turned over in some monomers in the crystal. However, ACS142 showed no evidence of turnover in a one-dimensional nuclear magnetic resonance assay with AnPRT, PRPP, and Mg^{2+} (data not shown).

Characterizing the Substrate Entrance Site as a Guide for Improved Inhibitor Design. On the basis of the observed binding modes of all the inhibitors, we can speculate about the relative importance of the residues that make up the anthranilate-binding site at the entrance of the tunnel. Hydrophobic interactions and/or π -interactions with Pro180 and Tyr186 were observed for all inhibitors, and this appears to be a major determinant of binding. Arg194, which is located on the outside of the enzyme, was frequently observed binding to inhibitors and may be involved in capturing ligands from solution by hydrogen bonding to their carboxyl groups. Neither Arg194 nor the two hydrophobic residues, Tyr186 and Pro180, are conserved in AnPRT enzymes from other species. However, the structure of *Sso*-AnPRT in complex with a substrate shows that anthranilate binds at the outer site through contacts with the hydrophobic side chain of Met151, and with His154, which could form π -interactions through its aromatic ring.^{7,10,11} These interactions may be comparable to those seen in *Mtb*-AnPRT. The equivalent histidine in *Mtb*-AnPRT (His183) forms hydrophobic contacts with all of the inhibitors (Table 2). Asn138 and Arg193 also appeared to be particularly important for binding at the outer site of the substrate-binding tunnel. These residues are conserved in other AnPRT enzymes, and their equivalents in the *Sso*-AnPRT are essential for enzyme activity.^{7,10} Interestingly, these residues were also involved in binding molecules farther into the active site. This raises the possibility that these two residues, which are capable of binding both polar substituents of an anthranilate molecule, function to shuttle substrate molecules from the outer binding site at the edge of the substrate-binding tunnel to the

inner catalytic site, following initial weak binding mediated by $CH\cdots\pi$ bonds^{37,38} with Tyr186 and Pro180.

These observations suggest routes for the design of further inhibitors. The inhibitors in this study illustrate that it is possible for a compound to be an effective inhibitor by occupying the outer binding site in the substrate-binding tunnel. Most of the inhibitory compounds that bind into the outer site do so without making many specific hydrogen bonds with the protein; instead, most of the contacts are due to the enclosure of an aromatic ring in the hydrophobic sandwich at the mouth of the substrate-binding tunnel, formed by Tyr186 and Ala190 on one side and Pro180 on the other. This makes the generation of a traditional pharmacophore problematic, as there is little chemical conservation among the inhibitors that bind into this site, beyond an aromatic ring. However, the binding modes of compounds ACS172, ACS174, and ACS179 suggest a strategy for future inhibitor design, in which an aromatic ring fits into the hydrophobic sandwich, and extended substituents on this ring then reach into the substrate-binding tunnel to make specific interactions with both Asn138 and Arg193.

The inhibitors described here show modest inhibition of AnPRT (low micromolar K_i values at best) and do not have chemical properties that are likely to be favorable for their uptake into mycobacterial cells. Hence, they are starting points for the structure-guided design of high-affinity inhibitors of AnPRT with chemical characteristics better suited to penetration of the mycobacterial cell wall. We are currently embarking on a program of improved inhibitor synthesis based on the structures presented in this paper.

CONCLUSION

New crystallization conditions have revealed a tunnel, ~ 15 Å in length, in the potential drug target *Mtb*-AnPRT when the enzyme is in its closed form. The closed form of the enzyme seems to be driven by the binding of its first substrate, PRPP, and the concurrent ordering of several loops. A new set of inhibitors of AnPRT with chemical characteristics similar to those of its second substrate, anthranilate, have been identified, along with detailed structural information about how these inhibitors bind to this enzyme. To the best of our knowledge, these are the first inhibitors of *Mtb*-AnPRT to be described. All were found to bind primarily at the entrance of the tunnel, rather than deeper inside the tunnel at the active site. Some of them, including the most potent, were also able to bind in positions deeper inside the tunnel. These results support previous findings^{10,13} that in AnPRT enzymes there is a second position for anthranilate to bind at the entrance of the tunnel leading to the active site and indicate the potential for taking advantage of this feature of AnPRT for further inhibitor design.

ASSOCIATED CONTENT

Supporting Information

Details of the inhibitor screening and enzymatic characterization (Figures S1 and S2), a figure describing ligand-induced changes in the protein structure (Figure S3), illustrations of electron density maps to support the modeling of the inhibitors (Figures S4 and S6), and details of crystallization conditions, structure refinement, and binding modes for the enzyme–inhibitor complexes (Tables S1–S3). This material is available free of charge via the Internet at <http://pubs.acs.org>.

AUTHOR INFORMATION

Corresponding Author

*E-mail: s.lott@auckland.ac.nz. Telephone: +64 9 923 7074.

Present Addresses

[§]Karolinska Institute, Department of Microbiology, Tumor and Cell Biology, 171 77 Stockholm, Sweden.

^{||}Department of Biochemistry, University of Cambridge, Tennis Court Road, Cambridge CB2 1QW, United Kingdom.

Author Contributions

A.C. and F.L.S. contributed equally to this work.

Author Contributions

J.S.L., A.C., and E.M.M.B. conceived and designed the experiments. F.L.S., A.C., T.V.M.C., D.D.A.J., and C.E.L. performed the experiments. A.C., F.L.S., G.L.E., E.M.M.B., and C.E.L. analyzed the data. A.C., F.L.S., and G.L.E. wrote the paper. A.C., F.L.S., G.L.E., T.V.M.C., E.M.M.B., C.E.L., E.J.P., E.N.B., and J.S.L. revised the paper.

Funding

This work was supported by funding from the Health Research Council of New Zealand, the Foundation for Research, Science and Technology of New Zealand and the Tertiary Education Commission of New Zealand through CoRE funding to the Maurice Wilkins Centre for Molecular Biodiscovery.

Notes

The authors declare no competing financial interest.

ACKNOWLEDGMENTS

We gratefully acknowledge Dr. Farah Javid-Majd and Prof. Jim Sacchettini (Department of Biochemistry and Biophysics, Texas A&M University, College Station, TX) for the *Mtb*-AnPRT expression plasmid. This work was performed as part of the *M. tuberculosis* Structural Genomics Consortium (<http://www.webtb.org>). We also gratefully acknowledge Dr. Jackie Kendall and Dr. Julie Spicer and Prof. Bill Denny (The Auckland Cancer Society Research Centre, Auckland, New Zealand) for providing the compounds for the targeted screen against *Mtb*-AnPRT.

ABBREVIATIONS

AnPRT, anthranilate phosphoribosyl transferase; *Eco*, *E. coli*; IPTG, isopropyl β -D-thiogalactopyranoside; K_i , inhibition constant; *Mtb*, *M. tuberculosis*; NP, nucleoside phosphorylases; *Pca*, *P. carotovorum*; PRA, N-(5'-phosphoribosyl)anthranilate; PRAI-InGPS, PRA isomerase-indoleglycerol phosphate synthase; PRPP, 5'-phosphoribosyl 1'-pyrophosphate; PRT, phosphoribosyl transferases; rmsd, root-mean-square difference; SeMet, selenomethionine; *Sso*, *S. solfataricus*.

REFERENCES

- (1) World Health Organization (2012) Global Tuberculosis Control 2011, Geneva.
- (2) World Health Organization (2010) Multidrug and extensively drug-resistant TB (M/XDR-TB): 2010 global report on surveillance and response, Geneva.
- (3) Smith, D. A., Parish, T., Stoker, N. G., and Bancroft, G. J. (2001) Characterization of auxotrophic mutants of *Mycobacterium tuberculosis* and their potential as vaccine candidates. *Infect. Immun.* 69, 1142–1150.
- (4) Musick, W. D. L. (1981) Structural Features of the Phosphoribosyl-Transferases and Their Relationship to the Human Deficiency Disorders of Purine and Pyrimidine Metabolism. *Crit. Rev. Biochem. Mol. Biol.* 11, 1–34.

- (5) Schramm, V. L., and Grubmeyer, C. (2004) Phosphoribosyl-transferase mechanisms and roles in nucleic acid metabolism. *Prog. Nucleic Acid Res. Mol. Biol.* 78, 261–304.
- (6) Bode, R. R., and Birnbaum, D. D. (1977) [Enzymes of aromatic amino acid biosynthesis in *Hansenula henricii*: Anthranilate phosphoribosylpyrophosphate-phosphoribosyltransferase (E.C.2.4.2.18)]. *Z. Allg. Mikrobiol.* 18, 559–566.
- (7) Mayans, O., Ivens, A., Nissen, L. J., Kirschner, K., and Wilmanns, M. (2002) Structural analysis of two enzymes catalysing reverse metabolic reactions implies common ancestry. *EMBO J.* 21, 3245–3254.
- (8) Pugmire, M. J., and Ealick, S. E. (2002) Structural analyses reveal two distinct families of nucleoside phosphorylases. *Biochem. J.* 361, 1–25.
- (9) Smith, J. L. (1999) Forming and inhibiting PRT active sites. *Nat. Struct. Mol. Biol.* 6, 502–504.
- (10) Lee, C. E., Goodfellow, C., Javid-Majd, F., Baker, E. N., and Lott, J. S. (2006) The crystal structure of TrpD, a metabolic enzyme essential for lung colonization by *Mycobacterium tuberculosis*, in complex with its substrate phosphoribosylpyrophosphate. *J. Mol. Biol.* 355, 784–797.
- (11) Kim, C., Xuong, N. H., Edwards, S., Madhusudan, Yee, M. C., Spragg, G., and Mills, S. E. (2002) The crystal structure of anthranilate phosphoribosyltransferase from the enterobacterium *Pectobacterium carotovorum*. *FEBS Lett.* 523, 239–246.
- (12) Verdonk, M. L., Chessari, G., Cole, J. C., Hartshorn, M. J., Murray, C. W., Nissink, J. W. M., Taylor, R. D., and Taylor, R. (2005) Modeling Water Molecules in Protein–Ligand Docking Using GOLD. *J. Med. Chem.* 48, 6504–6515.
- (13) Marino, M., Deuss, M., Svergun, D. I., Konarev, P. V., Sterner, R., and Mayans, O. (2006) Structural and mutational analysis of substrate complexation by anthranilate phosphoribosyltransferase from *Sulfolobus solfataricus*. *J. Biol. Chem.* 281, 21410–21421.
- (14) de Marco, A. (2011) Molecular and Chemical Chaperones for Improving the Yields of Soluble Recombinant Proteins. In *Heterologous Gene Expression in E. coli* (Evans, T. C., and Xu, M.-Q., Eds.) pp 31–51, Humana Press, Totowa, NJ.
- (15) Van Duyne, G. D., Standaert, R. F., Karplus, P. A., Schreiber, S. L., and Clardy, J. (1993) Atomic structures of the human immunophilin FKBP-12 complexes with FK506 and rapamycin. *J. Mol. Biol.* 229, 105–124.
- (16) Creighton, T. E., and Yanofsky, C. (1970) Chorismate to tryptophan (*Escherichia coli*) – anthranilate synthetase, PR transferase, PRA isomerase, InGP synthetase, tryptophan synthetase. *Methods Enzymol.* 17, 365–380.
- (17) Leatherbarrow, R. J. (2001) *GraFit*, version 5, Erithacus Software Ltd., Horley, U.K.
- (18) Moreland, N., Ashton, R., Baker, H. M., Ivanovic, I., Patterson, S., Arcus, V. L., Baker, E. N., and Lott, J. S. (2005) A flexible and economical medium-throughput strategy for protein production and crystallization. *Acta Crystallogr. D* 61, 1378–1385.
- (19) Vornrhein, C., Flensburg, C., Keller, P., Sharff, A., Smart, O., Paciorek, W., Womack, T., and Bricogne, G. (2011) Data processing and analysis with the autoPROC toolbox. *Acta Crystallogr. D* 67, 293–302.
- (20) Kabsch, W. (2010) XDS. *Acta Crystallogr. D* 66, 125–132.
- (21) Evans, P. (2006) Scaling and assessment of data quality. *Acta Crystallogr. D* 62, 72–82.
- (22) Otwinowski, Z., and Minor, W. (1997) Processing of X-ray diffraction data collected in oscillation mode. *Methods Enzymol.* 276, 307–326.
- (23) Vagin, A., and Teplyakov, A. (2010) Molecular replacement with MOLREP. *Acta Crystallogr. D* 66, 22–25.
- (24) Emsley, P., and Cowtan, K. (2004) Coot: Model-building tools for molecular graphics. *Acta Crystallogr. D* 60, 2126–2132.
- (25) Murshudov, G. N., Vagin, A. A., and Dodson, E. J. (1997) Refinement of macromolecular structures by the maximum-likelihood method. *Acta Crystallogr. D* 53, 240–255.
- (26) Blanc, E., Roversi, P., Vornrhein, C., Flensburg, C., Lea, S. M., and Bricogne, G. (2004) Refinement of severely incomplete structures with maximum likelihood in BUSTER-TNT. *Acta Crystallogr. D* 60, 2210–2221.

- (27) Schüttelkopf, A. W., and Van Aalten, D. M. F. (2004) PRODRG: A tool for high-throughput crystallography of protein-ligand complexes. *Acta Crystallogr. D60*, 1355–1363.
- (28) Engh, R. A., and Huber, R. (1991) Accurate Bond and Angle Parameters for X-ray Protein-Structure Refinement. *Acta Crystallogr. A47*, 392–400.
- (29) Chen, V. B., Arendall, W. B., Headd, J. J., Keedy, D. A., Immormino, R. M., Kapral, G. J., Murray, L. W., Richardson, J. S., and Richardson, D. C. (2010) MolProbity: All-atom structure validation for macromolecular crystallography. *Acta Crystallogr. D66*, 12–21.
- (30) The PyMOL Molecular Graphics System, Version 1.5.0.4 Schrödinger, LLC.
- (31) Ten Eyck, L. F. (1985) Fast Fourier transform calculation of electron density maps. *Methods Enzymol. 115*, 324–337.
- (32) Winn, M. D., Ballard, C. C., Cowtan, K. D., Dodson, E. J., Emsley, P., Evans, P. R., Keegan, R. M., Krissinel, E. B., Leslie, A. G. W., McCoy, A., McNicholas, S. J., Murshudov, G. N., Pannu, N. S., Potterton, E. A., Powell, H. R., Read, R. J., Vagin, A., and Wilson, K. S. (2011) Overview of the CCP4 suite and current developments. *Acta Crystallogr. D67*, 235–242.
- (33) Wallace, A. C., Laskowski, R. A., and Thornton, J. M. (1995) LIGPLOT: A program to generate schematic diagrams of protein-ligand interactions. *Protein Eng. 8*, 127–134.
- (34) Krissinel, E., and Henrick, K. (2004) Secondary-structure matching (SSM), a new tool for fast protein structure alignment in three dimensions. *Acta Crystallogr. D60*, 2256–2268.
- (35) Bauerle, R., Hess, J., and French, S. (1987) Anthranilate synthase-anthranilate phosphoribosyltransferase complex and subunits of *Salmonella typhimurium*. *Methods Enzymol. 142*, 366–386.
- (36) Chakrabarti, P., and Bhattacharyya, R. (2007) Geometry of nonbonded interactions involving planar groups in proteins. *Prog. Biophys. Mol. Biol. 95*, 83–137.
- (37) Brandl, M., Weiss, M. S., Jabs, A., Sühnel, J., and Hilgenfeld, R. (2001) C–H··· π -interactions in proteins. *J. Mol. Biol. 307*, 357–377.
- (38) Scheiner, S., Kar, T., and Pattanayak, J. (2002) Comparison of various types of hydrogen bonds. *J. Am. Chem. Soc. 124*, 13257–13264.
- (39) Burley, S. K., and Petsko, G. A. (1986) Amino-aromatic interactions in proteins. *FEBS Lett. 203*, 139–143.